

Lynds Bright Nebulae: Sites of possible twisted filaments and ongoing star formation

L. K. Dewangan^{1*}, J. S. Dhanya², N. K. Bhadari^{1,3}, D. K. Ojha⁴, and T. Baug⁵

¹Physical Research Laboratory, Navrangpura, Ahmedabad - 380 009, India.

²Malaviya National Institute of Technology (MNIT), Jaipur 302017, Rajasthan, India.

³Indian Institute of Technology Gandhinagar Palaj, Gandhinagar, 382355, India.

⁴Department of Astronomy and Astrophysics, Tata Institute of Fundamental Research, Homi Bhabha Road, Mumbai 400 005, India.

⁵Satyendra Nath Bose National Centre for Basic Sciences, Block-JD, Sector-III, Salt Lake, Kolkata-700 106, India.

ABSTRACT

The paper presents an analysis of multi-wavelength data of two Lynds Bright Nebulae (LBN), LBN 140.07+01.64 and LBN 140.77–1.42. The 1420 MHz continuum map reveals an extended Y-shaped feature (linear extent $\sim 3^\circ.7$), which consists of a linear part and a V-like structure. The sites LBN 140.07+01.64 and AFGL 437 are located toward the opposite sides of the V-like structure, and LBN 140.77–1.42 is spatially seen toward the linear part. Infrared-excess sources are traced toward the entire Y-feature, suggesting star formation activities. Infrared and sub-millimeter images show the presence of at least two large-scale dust filaments extended toward the LBN sources. The *Herschel* maps, which are available only toward the northern and central parts of the Y-feature, display the presence of higher column density ($\geq 2.4 \times 10^{21} \text{ cm}^{-2}$) of materials toward the filaments. Using the $^{12}\text{CO}(1-0)$ line data, the distribution of molecular gas at $[-42.7, -34.4] \text{ km s}^{-1}$ traces the cloud associated with the Y-feature, and confirms the existence of filaments. The large-scale filaments appear to be possibly spatially twisted. There is a hint of an oscillatory-like velocity pattern along both the filaments, favouring their proposed twisted nature. It is the first study showing the possible twisting of filaments, which is more prominent in the northern and central parts of the Y-feature. This possible twisting/coupling of the large-scale filaments appears to be responsible for the observed star formation (including known OB-stars). The proposed physical process and the energetics of OB-stars together seem to explain the origin of the ionized Y-feature.

Key words: dust, extinction – HII regions – ISM: clouds – ISM: individual object (LBN 140.77–1.42, LBN 140.07+1.64) – stars: formation – stars: pre-main sequence

1 INTRODUCTION

In the last decade, the study of infrared (IR) and sub-millimeter (sub-mm) observations revealed that filaments are common structures in low-mass and high-mass star-forming regions and their role in the star formation processes has been evident (e.g., Myers 2009; André et al. 2010; Dewangan et al. 2015, 2017b, 2018, 2019, 2020; Dewangan 2021; Tigé et al. 2017; Motte et al. 2018; Treviño-Morales et al. 2019; Kumar et al. 2020). In this context, one can study the signatures of the convergence of filaments toward the compact and dense hub, the intersection/merging of filaments, and the collisions of filaments, which can explain the ongoing physical processes in star-forming regions. In

such events/scenarios, the highest column density can be observed in the interaction zones of filaments. Additionally, a filament braid, where continuous multiple filaments are twisted, could also be considered as one of the interesting star-forming sites. In such configuration, multiple common zones with high column densities are expected. However, in the literature, we do not find any promising star-forming sites where the twisting of filaments is investigated. In this relation, the target of our present paper is two Lynds Bright Nebulae (LBN), LBN 140.07+01.64 and LBN 140.77–1.42 (Lynds 1965; Green 1989; Karr & Martin 2003a).

LBN 140.77–1.42 has been investigated as a linear radio ridge (extent $\sim 2^\circ$; Green 1989), while LBN 140.07+1.64 has a more diffuse appearance in the radio 1420 MHz continuum map (Karr & Martin 2003a). The radio emission detected toward both the LBN sources was found to be thermal in na-

* lokeshd@prl.res.in

ture (Green 1989; Karr & Martin 2003a). The molecular gas at $V_{\text{lsr}} = [-45.2, -32.8]$ km s $^{-1}$ and the dust emission were traced toward the LBN sources (Heyer et al. 2001; Karr & Martin 2003a). Using the molecular line data (i.e., $^{12}\text{CO}(1-0)$, $^{13}\text{CO}(1-0)$, and $\text{C}^{18}\text{O}(1-0)$) from the Purple Mountain Observatory Delingha (PMODLH) 13.7 m telescope, Du et al. (2017) also studied the molecular emission toward an area containing both the LBN sources, which was designated as “Grand Canal” (see Figure 10 in their paper). The Grand Canal was reported as a giant filamentary molecular cloud (GFMC) in the Perseus Arm (Du et al. 2017), and was divided into three parts (see also IDs 50–52 in Digel et al. 1996). Karr & Martin (2003a) identified young stellar objects (YSOs) based on the IRAS color conditions, which were found toward the Grand Canal hosting the LBN sources (see Figure 3 in their paper).

Figure 1a shows the radio 1420 MHz continuum map of an area containing LBN 140.07+01.64 and LBN 140.77–1.42. The positions of a few known star-forming sites/HII regions (i.e., IRAS 03035+5819/AFGL 437, AFGL 5090, IRAS 03101+5821, and IRAS 03063+5735) are also indicated in Figure 1a. The positions of molecular clumps (from Heyer et al. 2001) are also overlaid on the 1420 MHz continuum map, and are shown only for the area where the extended ionized emission is detected in the radio map at 1420 MHz (see a dotted-dashed box in Figure 1a). The kinematic distance of each molecular clump was also computed by Heyer et al. (2001), and the mean kinematic distance is found to be ~ 4.1 kpc. The distance of ~ 4.1 kpc was adopted for some known star-forming regions (i.e., AFGL 5090, AFGL 437, IRAS 03063+5735; Snell et al. 1988; Harju et al. 1998; Kobulnicky et al. 2012). Du et al. (2017) adopted a distance of ~ 2.1 kpc for the GFMC Grand Canal located in the Perseus Arm, and a distance of ~ 3 kpc was used by Green (1989). On the other hand, Karr & Martin (2003a) assumed a distance of ~ 2.0 kpc to both the LBN sources, which is a similar distance and V_{lsr} (i.e., -39 km s $^{-1}$) of nearby W3/W4/W5 regions (e.g., Karr & Martin 2003b; Navarete et al. 2019). Hence, following the work of Karr & Martin (2003a) and Du et al. (2017), we consider the distance of ~ 2 kpc to both the LBN sources in this work.

Based on the previous published works, we find that the identification of embedded filaments and their involvement in the ongoing physical mechanisms are yet to be performed in the GFMC hosting both the LBN sources, where the existence of high-mass OB-stars has been reported. In this relation, we examine the IR, sub-mm, and molecular maps to study the physical environments of LBN 140.07+01.64 and LBN 140.77–1.42. The high resolution near-infrared (NIR) photometric data have been employed to study the distribution of YSOs. Furthermore, we also explore the possible physical process responsible for the existence of the extended ionized nebulae, which has not yet been thoroughly investigated.

The multi-wavelength data sets are introduced in Section 2. The study of the embedded filaments and physical environment of the target site is performed in Section 3. Section 4 covers the implications of our observed findings. Section 5 summarizes the main results of our study.

2 DATA SETS

The present work deals mainly with a target area of $\sim 1^\circ.96 \times 4^\circ$ (central coordinates: $l = 140^\circ.55$; $b = -0^\circ.461$) in the direction of the extended ionized emission hosting LBN 140.07+01.64 and LBN 140.77–1.42 (see a dotted-dashed box in Figure 1a). We studied observational data sets collected from different Galactic plane surveys, which are listed in Table 1.

We also examined the *Herschel* temperature and column density maps (resolution $\sim 12''$), which are not available for the entire selected target area. Using the *Herschel* continuum images at 70–500 μm (Molinari et al. 2010a), the *Herschel* temperature and column density maps were produced for the *EU-funded ViaLactea project* (Molinari et al. 2010b). The Bayesian *PPMAP* procedure (Marsh et al. 2015, 2017) was adopted to produce these *Herschel* maps.

3 RESULTS

3.1 Extended ionized Y-shaped feature and its multi-wavelength view

In the direction of our selected target area, the CGPS 1420 MHz continuum image has allowed us to identify an extended Y-shaped morphology (hereafter, Y-feature; linear extent $\sim 3^\circ.7$ or ~ 129 pc at a distance of 2 kpc), which consists of a linear part and a V-like structure (see Figure 1a). The Y-feature is traced with the CGPS 1420 MHz continuum emission contour level of 5.5 K ($1\sigma \sim 71 \sin \delta$ mK; Taylor et al. 2003). The site LBN 140.77–1.42 is spatially seen toward the linear part of the Y-feature, while the sites LBN 140.07+01.64 and AFGL 437 are located toward the opposite sides of the V-like structure. We also find the spatial distribution of molecular clumps at $[-43, -34]$ km s $^{-1}$ (from Heyer et al. 2001) toward the entire Y-feature, confirming its physical existence (see also Section 3.2.1). The previously reported GFMC Grand Canal (e.g., Du et al. 2017) is seen toward the ionized Y-feature. However, the site AFGL 437 is spatially located away from the GFMC.

Figure 1b shows the WISE image at 12 μm of an area containing the Y-feature, displaying the presence of warm dust emission and large-scale filaments extended toward both the LBN sources. In our selected target area, the WISE map is available only for a latitude range of $[-1^\circ.6, 1^\circ.5]$. Based on the visual inspection of the WISE image, three subregions, sm1, sm2, and sm3 are chosen toward the northern, central, and southern parts of the Y-feature, respectively. In the WISE image, the southern part (i.e., sm3) of the Y-feature is seen with higher intensity than the northern and central parts.

To further examine the embedded filaments, Figure 2a presents the *Herschel* image at 160 μm toward an area hosting the sites AFGL 437, IRAS 03101+5821, and IRAS 03063+5735 (see a dotted-dashed box in Figure 1b). The areas of two subregions (i.e., sm1 and sm2) are also indicated in Figure 2a. Note that the *Herschel* observations partially cover the area of subregion sm2, and do not cover the southern part (i.e., sm3) of the Y-feature. At least three filaments (i.e., F1, F2, and F3) are spatially seen toward the subregion sm1, and two of them (i.e., F1 and F2) are also extended toward the subregion sm2 (see arrows in Figure 2a). We

Table 1. List of different surveys studied in this paper.

| Survey | Wavelength/Frequency/line(s) | Resolution | Reference |
|---|------------------------------|---------------------------------|-------------------------|
| Canadian Galactic Plane Survey (CGPS) | 1.42 GHz | $1' \times 1' \text{csc}\delta$ | Taylor et al. (2003) |
| NRAO VLA Sky Survey (NVSS) | 1.4 GHz | $\sim 45''$ | Condon et al. (1998) |
| CGPS $^{12}\text{CO}(J=1-0)$ | 2.6 mm | $\sim 100''/4$ | Taylor et al. (2003) |
| <i>Herschel</i> Infrared Galactic Plane Survey (Hi-GAL) | 160 μm | $12''$ | Molinari et al. (2010a) |
| Wide-field Infrared Survey Explorer (WISE) | 12 μm | $\sim 6''.5$ | Wright et al. (2010) |
| UKIDSS Galactic Plane Survey (GPS) | 1.25–2.2 μm | $\sim 0''.8$ | Lawrence et al. (2007) |
| Two Micron All Sky Survey (2MASS) | 1.25–2.2 μm | $\sim 2''.5$ | Skrutskie et al. (2006) |

also see overlapping areas of the filaments F1 and F2 in the *Herschel* image at 160 μm . The quantitative information of the embedded features can be examined in Figure 2b. The site AFGL 437 is associated with the extended 160 μm continuum emission, and is known to host an H II region (see Kumar Dewangan & Anandarao 2010). In the direction of AFGL 437, the spatial appearance of the 160 μm continuum emission is very similar as seen in the *Spitzer* image at 8.0 μm (see Figure 1 in Kumar Dewangan & Anandarao 2010).

Figure 2b displays the *Herschel* column density map (resolution $\sim 12''$; Marsh et al. 2015, 2017) of an area highlighted by a solid box in Figure 1b. The column density contour ($N(\text{H}_2)$) at $2.4 \times 10^{21} \text{ cm}^{-2}$ is also shown in Figure 2b, indicating the presence of higher $N(\text{H}_2)$ of materials toward the filaments and the site AFGL 437.

3.2 Molecular structures

3.2.1 Moment-0 and Moment-1 maps

In this section, we examined the CGPS $^{12}\text{CO}(1-0)$ line data to study the distribution of molecular gas toward the Y-feature. The $^{12}\text{CO}(1-0)$ emission toward our target area is studied in a velocity range of $[-42.7, -34.4] \text{ km s}^{-1}$, allowing us to generate the integrated intensity (or moment-0) map and the intensity weighted mean velocity (or moment-1) map. For the moment-1 map, the molecular emission is clipped with a value of 3.9 K.

The moment-0 and moment-1 maps of the $^{12}\text{CO}(1-0)$ emission are presented in Figures 3a and 3b, respectively. The areas of three subregions (i.e., sm1, sm2, and sm3) are also marked in the moment-0 map, and are located toward the previously reported GFMC Grand Canal (i.e., a continuous elongated structure; see Figure 10 in Du et al. 2017). In the direction of sm3, a compact gas condensation is traced around AFGL 5090, which is surrounded by two arc-like molecular features. The arc-like molecular feature located toward the right side of AFGL 5090 has a filamentary appearance, where the diffuse dust emission is evident in the WISE image. In the moment-1 map, the gas velocity difference is evident toward the molecular structures traced in the moment-0 map. The blue-shifted molecular gas around -41 km s^{-1} is seen toward the subregion sm3, while the red-shifted gas around -36 km s^{-1} is depicted toward the subregion sm1 (see Figure 3b). This argument is also supported by the examination of the published position-velocity diagram of molecular gas (see Figure 10g in Du et al. 2017). In the direction of AFGL 437, a noticeable velocity variation is also evident, which may suggest the presence of an outflow activity. It is in agreement with the previously reported

IR outflow in AFGL 437 (Kumar Dewangan & Anandarao 2010).

To further explore the distribution of molecular gas, in Figure 4, we present velocity channel maps of $^{12}\text{CO}(1-0)$, where the positions of star-forming sites are also marked by star symbols. Figure 4 confirms the existence of a continuous elongated molecular structure in the direction of the Y-feature. The molecular gas is evident toward the *Herschel* dust filaments (i.e., F1, F2, and F3; see Figure 2a). It also appears that the filaments F1 and F2 are large scale molecular structures, and are present in all the subregions (i.e., sm1, sm2, and sm3; see Figures 4c–4f). It is interesting to note that Figure 4f traces the two curved and coupled filaments (i.e., F1 and F2) in the northern direction.

To spatially outline the molecular filaments, Figure 5a presents a two-color composite map (red: *IDL* based routine “sobel” processed moment-0 map, turquoise: moment-0 map) of an area hosting all the subregions (i.e., the GFMC Grand Canal) excluding the site AFGL 437. The sobel filter is often utilized for edge detection (Sobel 2014), allowing us to uncover the molecular filaments in the Y-feature. The sobel filter finds the edges by seeking for the minimum and maximum in the first derivative of the input image (Sobel 2014). For a comparison, Figure 5b shows the IR image of the same area as seen in Figure 5a. In Figure 5b, the *Herschel* 160 μm image (in turquoise color) covers the subregions sm1 and sm2, and the WISE 12 μm image (in red) is shown toward the subregion sm3. In Figure 5a, the filaments F1 and F2 seem to be coupled to each other, revealing a twisted behaviour. However, the filament F3 appears as a separate branch. To further confirm the possible twisted nature of the filaments, the knowledge of the velocity structure along each filament is required. The coupled filamentary features can also be seen in the direction of subregions sm2 and sm3, but they are not as prominent as seen in the subregion sm1 (see also Figure 5b).

3.2.2 Velocity structures of the filaments

To further explore the filaments, F1–F3, a zoomed-in view of the area containing the subregion sm1 is presented in Figure 6. Figures 6a and 6b present the *Herschel* temperature and column density maps of the subregion sm1, respectively. In Figures 6c and 6d, we show the ^{12}CO moment-0 map at $[-42.7, -34.4] \text{ km s}^{-1}$ and the moment-1 map of the subregion sm1, respectively. In the *Herschel* maps, we find the filaments (i.e., F1, F2, and F3) with T_d of $\sim 13\text{--}15 \text{ K}$ and $N(\text{H}_2) \sim 2.4\text{--}10 \times 10^{21} \text{ cm}^{-2}$. Each molecular filament is highlighted by a curve in Figure 6c, where several small circles (radii $\sim 20''$) are also marked. We examined an average spectrum over each circle, and obtained a peak velocity

through the fitting of the observed spectrum with a Gaussian function. The star-forming site IRAS 03101+5821 is located toward either filament F1 or F2. In Figure 6d, one can also find the noticeable gas velocity difference of about 2-3 km s⁻¹ toward the filaments F1 and F2. The filament F3, which appears as an adjacent filamentary branch, also shows considerable velocity difference.

Figures 7a, 7b, and 7c present the position-velocity diagrams along the filaments F1, F2, and F3, respectively (see curves shown in Figure 6c). The majority of the molecular gas in the direction of the filaments F1 and F2 is traced in a velocity range of [-36, -41] km s⁻¹, while the majority of the molecular gas toward the filament “F3” is depicted in a velocity range of [-35, -39] km s⁻¹. In Figures 7a and 7b, the common zones of the filaments F1 and F2 are highlighted by pink boxes (see also arrows in Figure 6c). We find a velocity gradient of about 0.3–0.5 km s⁻¹ pc⁻¹ toward these common zones. The common zones of the filaments are also associated with a relatively high intensity compared to their other parts. From Figures 6c and 7, the spatial extension of the common zones is found to be about 6′–8′ (or ~3.5–4.6 pc). The observed high intensities and velocity gradient toward the common zones suggest the possible interaction between both the filaments. However, we do not find such an intensity variation along the filament F3.

The coarse beam of the CGPS ¹²CO(1–0) line data does not allow us to get more insights into the velocity structures of the filaments. However, based on a visual examination, there is a hint of an oscillatory-like velocity pattern along both the filaments F1 and F2, showing velocity variations. To further examine this aspect, we display mean velocities (along with error bars) of averaged spectra over circular regions as highlighted along each filament (see circles in Figure 6c). This particular analysis indicates the presence of the oscillatory-like velocity pattern along the filaments F1 and F2, but it is not clearly seen in the case of F3. Furthermore, this velocity pattern is more obvious in the case of F2 compared to F1. The implication of this finding is discussed in Section 4.

3.3 Star formation activities

To infer the infrared-excess sources/YSOs toward the Y-feature, we examined a color-magnitude (H–K/K) diagram of point-like sources detected in the H and K bands. In this relation, we used the reliable H- and K-band photometric data from the UKIDSS-GPS and 2MASS surveys. Detailed procedures for the selection of H and K sources are given in Lucas et al. (2008) and Dewangan et al. (2015, 2017a). A color condition of H–K > 1.3 mag is chosen to identify the YSO candidates, and is found through the study of the color-magnitude space of a nearby control field. A total of 80 YSO candidates are selected in the direction of Y-feature. In Figure 8a, the positions of the selected YSO candidates are overlaid on the moment-0 map of ¹²CO (see circles). A large number of YSOs are seen toward the site AFGL 5090, while the site AFGL 437 hosts a few YSOs. Figure 8b displays the locations of previously known YSOs (see squares) overlaid on the ¹²CO map, which were identified using the IRAS color conditions (from Karr & Martin 2003a). The NVSS 1.4 GHz continuum emission contours are also overlaid on

the ¹²CO map, allowing us to infer the locations of the H II regions toward the Y-feature.

We find ongoing star formation activities toward the entire Y-feature, which hosts LBN 140.07+01.64, LBN 140.77–1.42, and some previously reported star-forming sites/H II regions (i.e., IRAS 03035+5819/AFGL 437, AFGL 5090, IRAS 03101+5821, and IRAS 03063+5735). From Figures 8a and 8b, noticeable YSO candidates are also inferred toward the common zones of the filaments F1 and F2, where high column densities are depicted in the *Herschel* column density map (see Figure 2b).

Taking all these results together, high-mass OB-stars and YSOs are present in the Y-feature.

4 DISCUSSION

We identified a large-scale ionized Y-feature (linear extent ~3°.7 or ~129 pc at a distance of 2 kpc) located in the Perseus Arm (see Figure 1a). Furthermore, the IR, sub-mm, and molecular line data have revealed at least two large-scale filaments (F1 and F2) in the Y-feature (see Section 3.2). The linear extension of each filament is more than 20 pc. The spatial appearance of these filaments hints their coupling nature, revealing several possible overlapping zones of high column densities. The filamentary twisting/coupling appears more significant in the northern and central areas of the Y-feature. The initial assessment of twisting/coupling of the filaments is performed on the two-dimensional (2D) images, but a twisted shape is a three-dimensional (3D) morphology. Therefore, we have studied the velocity structures of the filaments using the CGPS ¹²CO line data (see Section 3.2.2), which have a coarse beam size (see Table 1). In this relation, the position-velocity diagrams along the filaments are examined, and reveal a signature of an oscillatory-like velocity pattern along each filament, separately (see Figures 7a and 7b). Note that in this work, we are dealing with two spatially coupled filaments. Hence, in general, one may expect such an oscillation-like velocity pattern, which may be related to the possible twisted behaviour. However, a physical model is required to successfully explain the observed spatial and velocity structures, and such a study is beyond the scope of this work.

Concerning this underlying velocity structure, in the literature, we find a promising filament G350.5-N associated with the cloud G350.54+0.69, where a large-scale periodic velocity oscillation was reported by Liu et al. (2019) using the ¹³CO(2–1) and C¹⁸O(2–1) line data (resolution ~28″; see Figures 6 and 7 in their paper). This observed velocity structure was suggested to be originated from the combined effects of core/fragment formation (e.g., Kainulainen et al. 2016; Dewangan et al. 2019) and the large-scale physical oscillation along the filament (see Liu et al. 2019, for more details). Based on our study presented in this paper, we suggest that the observed velocity structure along the filaments, F1 and F2, may be related to large-scale physical oscillations, and hints their possible twisted behaviour. High-resolution continuum and molecular line observations will be helpful to further explore the twisted filaments in the Y-feature. Considering these results, we suggest that it is the first observational work reporting the possible twist-

ing of the large-scale molecular and dust filaments, which is the most striking outcome of this work.

The involvement of embedded filaments in star formation processes (including low- and high-mass stars) has been known in the literature. In this relation, signposts of star formation activities are largely investigated at the intersection/merging/collision zones of filaments as well as the junction of multiple parsec scale filaments (i.e., hub-filament system; Myers 2009; Motte et al. 2018). Most recently, a theoretical study on merging filaments has been carried out (Hoemann et al. 2021, submitted to MNRAS). Hoemann et al. (2021) studied the merging behavior of parallel aligned filaments. On the other hand, in the case of isolated filaments, the end-dominated collapse (EDC) process has been proposed, and favours the fragmentation and collapse at the ends of the filaments (Pon et al. 2012; Clarke & Whitworth 2015). However, the twisting of filaments is an uncommon phenomenon, and has not been introduced in the literature so far. In systems hosting the twisting of filaments, one may expect multiple overlapping areas of high column density regions, where star formation may proceed. Hence, the follow up theoretical studies are highly essential to explore the role of twisting and coupling of filaments in star formation processes.

We find the presence of high-mass OB-stars and YSOs in the direction of the Y-feature (see Section 3.3), showing signs of ongoing star formation. In particular, in the northern part of the Y-feature, noticeable YSOs are found toward the possible common zones of the filaments, F1 and F2 (see circles in Figure 8a and squares in Figure 8b). On a global scale of the Y-feature, the star formation seems to be guided by the large-scale coupling and twisted nature of filaments.

Previously, it was proposed that LBN 140.77–1.42 may be a large-scale ionization front penetrating a large interstellar cloud (Green 1989). Later, Karr & Martin (2003a) suggested that the ionized material in both the LBN sources could be illuminated by the emission from a nearby high-mass O-star HD 16691 and the ultra-violet (UV) photons from W5 and W3/W4 regions. Hence, it is possible that the origin of the large-scale Y-feature may be influenced by the energetics of high-mass stars (i.e., ionized emission, stellar wind, and radiation pressure), but stellar feedback from the nearby high-mass stars/complexes may not be the only mechanism to explain the origin of the large-scale Y-feature. Some other physical process may be ongoing in the Y-feature, which could explain its origin. In this context, the role of the molecular and dust filaments is very promising. We suggest that the large-scale coupling and twisting of filaments might have formed the low-mass and high-mass stars. Additionally, the influence of the previously known high-mass stars to their immediate surroundings cannot be ruled out.

Overall, our proposed physical process has a significant contribution to explain the existence of the ionized Y-feature and the observed star formation activities.

5 SUMMARY AND CONCLUSIONS

This paper uses multi-wavelength and multi-scale data to study morphology and kinematics of the gas toward the two Lynds Bright Nebulae, LBN 140.07+01.64 and

LBN 140.77–1.42. Both the LBN sources are found to be a part of a large scale ionized Y-feature (linear extent $\sim 3^\circ.7$ or ~ 129 pc at a distance of 2 kpc) that is identified in the CGPS 1420 MHz continuum map. The previously identified star-forming sites/HII regions (i.e., IRAS 03035+5819/AFGL 437, AFGL 5090, IRAS 03101+5821, and IRAS 03063+5735) are spatially seen in the direction of Y-feature, hosting high-mass OB-stars. Infrared-excess sources/YSOs are found in the direction of the entire Y-feature, enabling us to infer the ongoing star formation activities. The inspection of the IR and sub-mm images reveals at least two large-scale dust filaments extended toward both the LBN sources. In the direction of the northern and central parts of the Y-feature, the *Herschel* column density and temperature maps display higher column density ($\geq 2.4 \times 10^{21} \text{ cm}^{-2}$) of materials toward the filaments with the dust temperature of ~ 13 – 15 K. The CGPS $^{12}\text{CO}(1-0)$ line data depict the large-scale filamentary structures toward the Y-feature, which are investigated in a velocity range of $[-42.7, -34.4] \text{ km s}^{-1}$. The molecular and dust filaments seem to be twisted and coupled to each other, showing several possible overlapping zones of high column densities. In the northern part of the Y-feature, the study of the velocity structures of the filaments also indicates their possible twisted nature.

For the first time, the present paper observationally reports the possible twisting/coupling of the large-scale filaments. This underlying mechanism and the energetics of high-mass OB-stars together appear to be responsible for the origin of the ionized Y-feature.

ACKNOWLEDGMENTS

We thank the anonymous reviewer for several useful comments and suggestions, which greatly improved the scientific contents of the paper. The research work at Physical Research Laboratory is funded by the Department of Space, Government of India. The research presented in this paper has used data from the Canadian Galactic Plane Survey, a Canadian project with international partners, supported by the Natural Sciences and Engineering Research Council. This work is based on data obtained as part of the UKIRT Infrared Deep Sky Survey. This publication makes use of data products from the Two Micron All Sky Survey, which is a joint project of the University of Massachusetts and the Infrared Processing and Analysis Center/California Institute of Technology, funded by the National Aeronautics and Space Administration and the National Science Foundation. TB acknowledges the support from S. N. Bose National Centre for Basic Sciences under the Department of Science and Technology (DST), Govt. of India. DKO acknowledges the support of the Department of Atomic Energy, Government of India, under project Identification No. RTI 4002.

Data availability

The CGPS 1420 MHz continuum map and $^{12}\text{CO}(1-0)$ line data underlying this article are available from the publicly accessible website¹. The NVSS 1.4 GHz continuum data un-

¹ <https://www.cadc-ccda.hia-ihp.nrc-cnrc.gc.ca/en/jcmt/>

derlying this article are available from the publicly accessible website². The *Herschel*, WISE, and 2MASS data underlying this article are available from the publicly accessible NASA/IPAC infrared science archive³. The *Herschel* column density and temperature maps underlying this article are available from the publicly accessible website⁴. The UKIDSS GPS data underlying this article are available from the publicly accessible website⁵.

REFERENCES

- André P. et al., 2010, *A&A*, 518, L102
 Clarke S. D., Whitworth A. P., 2015, *MNRAS*, 449, 1819
 Condon J. J., Cotton W. D., Greisen E. W., Yin Q. F., Perley R. A., Taylor G. B., Broderick J. J., 1998, *AJ*, 115, 1693
 Dewangan L. K., Luna A., Ojha D. K., Anandarao B. G., Mallick K. K., Mayya Y. D., 2015, *ApJ*, 811, 79
 Dewangan L. K., Ojha D. K., Zinchenko I., Janardhan P., Luna A., 2017a, *ApJ*, 834, 22
 Dewangan L. K., Baug T., Ojha D. K., Janardhan P., Devaraj R., Luna A., 2017b, *ApJ*, 845, 34
 Dewangan L. K., Baug T., Ojha D. K., Ghosh S. K., 2018, *ApJ*, 869, 30
 Dewangan L. K., Pirogov L. E., Ryabukhina O. L., Ojha, D. K., Zinchenko I., 2019, *ApJ*, 877, 1
 Dewangan L. K., Ojha D. K., Sharma Saurabh, del Palacio S., Bhadari N. K., Das A., 2020, *ApJ*, 903, 13
 Dewangan L. K., 2021, *MNRAS*, 504, 1152
 Digel S. W., Lyder D. A., Philbrick A. J., Puche D., Thaddeus P., 1996, *ApJ*, 458, 561
 Du X., Xu Y., Yang J., Sun Y., 2017, *ApJS*, 229, 24
 Green D. A., 1989, *AJ*, 98, 2210
 Harju J., Lehtinen K., Booth R. S., Zinchenko I., 1998, *A&AS*, 132, 211
 Heyer M. H., Carpenter J. H., Snell R. L., 2001, *ApJ*, 551, 852
 Hoemann E., Heigl S., Burkert A., 2021, preprint (arXiv:210404541)
 Kainulainen J., Hacar A., Alves J., Beuther H., Bouy H., Tafalla M., 2016, *A&A*, 586, 27
 Karr J. L., Martin, P. G., 2003a, *ApJ*, 595, 880
 Karr J. L., Martin, P. G., 2003b, *ApJ*, 595, 900
 Kobulnicky H. A., Lundquist M. J., Bhattacharjee A., Kerton C. R., 2012, *AJ*, 143, 71
 Kumar Dewangan L., Anandarao B. G., 2010 *MNRAS* 402 2583
 Kumar M. S. N., Palmeirim P., Arzoumanian D., Inutsuka S. I., 2020, *A&A*, 642, A87
 Lawrence A. et al., 2007, *MNRAS*, 379, 1599
 Liu H.-L., Stutz A., Yuan J.-H., 2019, *MNRAS*, 487, 1259
 Lucas P. W. et al., 2008, *MNRAS*, 391, 136
 Lynds B. T., 1965, *ApJS*, 12, 163
 Marsh K. A., Whitworth A. P., Lomax O., 2015, *MNRAS*, 454, 4282
 Marsh K. A. et al., 2017, *MNRAS*, 471, 2730
 Molinari S. et al., 2010a, *A&A*, 518, L100
 Molinari S. et al., 2010b, *PASP*, 122, 314
 Motte F., Bontemps S., Louvet F., 2018, *ARA&A*, 56, 41
 Myers P. C., 2009, *ApJ*, 700, 1609
 Navarete, F., Galli, P. A. B., Daminieli, A., 2019, *MNRAS*, 487, 2771
 Pon A., Toalá J. A., Johnstone D., Vázquez-Semadeni E., Heitsch F., Gómez G. C., 2012, *ApJ*, 756, 145
 Skrutskie M. F. et al., 2006, *AJ*, 131, 1163
 Snell R. L., Huang, Y. -L., Dickman R. L., Claussen M. J., 1988, *ApJ*, 325, 853
 Sobel, I., 2014. An Isotropic 3x3 Image Gradient Operator. Presentation at Stanford A.I. Project, p. 1968 (link: [http://refhub.elsevier.com/S0892-6875\(21\)00057-1/h0260](http://refhub.elsevier.com/S0892-6875(21)00057-1/h0260))
 Taylor A. R. et al., 2003, *AJ*, 125, 3145
 Tigé J. et al., 2017, *A&A*, 602, A77
 Treviño-Morales S. P. et al., 2019, *A&A*, 629, A81
 Wright E. L. et al., 2010, *AJ*, 140, 1868

² <https://www.cv.nrao.edu/nvss/postage.shtml>

³ <https://irsa.ipac.caltech.edu/frontpage/>

⁴ <http://www.astro.cardiff.ac.uk/research/ViaLactea/>

⁵ <http://wsa.roe.ac.uk/>

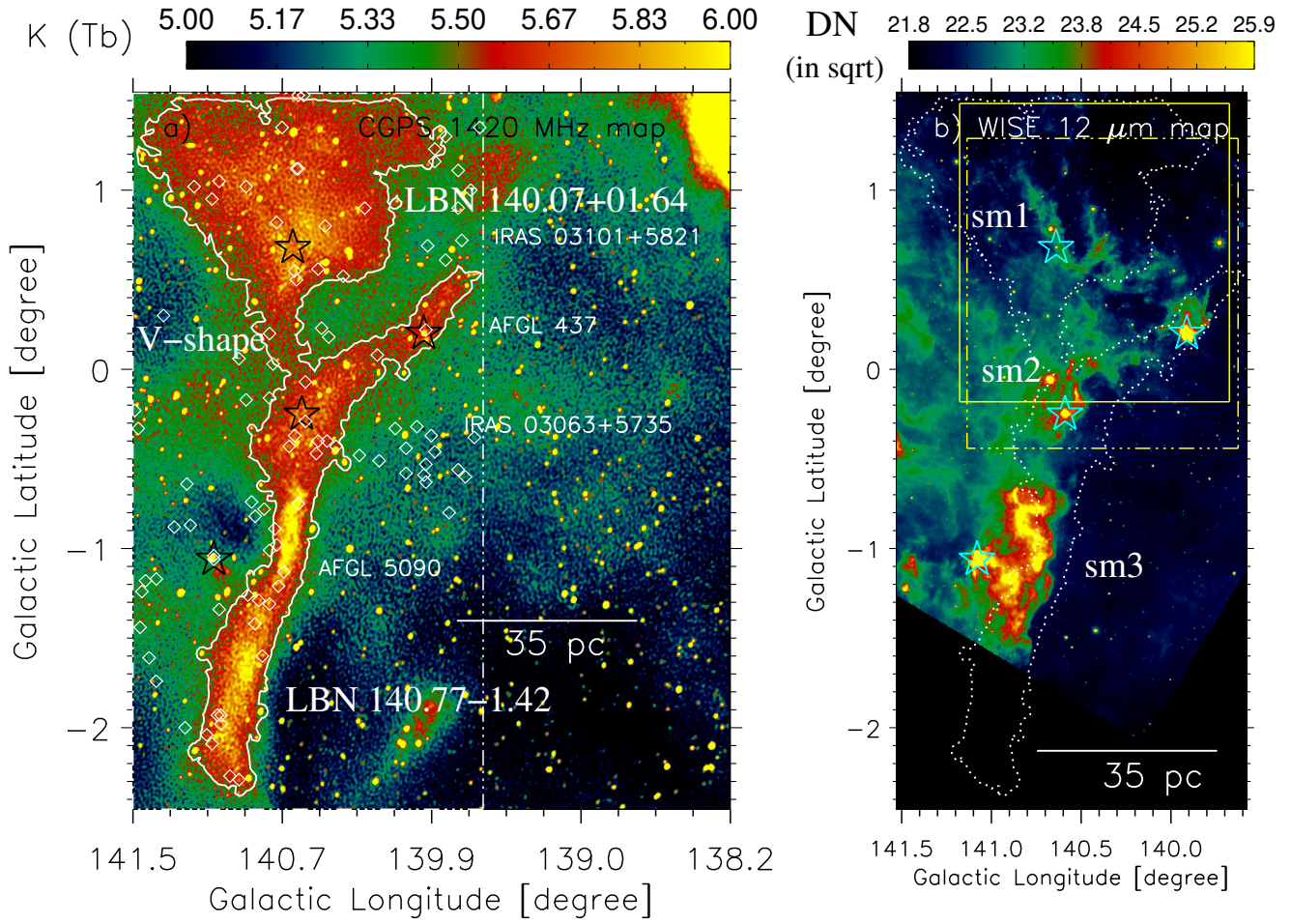


Figure 1. a) The panel shows the CGPS 1420 MHz continuum image (area $\sim 3^{\circ}.35 \times 4^{\circ}$; central coordinates: $l = 139^{\circ}.86$; $b = -0^{\circ}.469$). The CGPS 1420 MHz continuum emission contour at 5.5 K ($1\sigma \sim 71 \sin \delta$ mK; Taylor et al. 2003) traces the Y-feature. The positions of molecular clumps (from Heyer et al. 2001) are also shown by diamonds. b) WISE 12 μm image (area $\sim 1^{\circ}.96 \times 4^{\circ}$; central coordinates: $l = 140^{\circ}.55$; $b = -0^{\circ}.461$) in the direction of Y-feature (see a dotted-dashed box in Figure 1a). A dotted-dashed box highlights an area presented in Figure 2a, while a solid box encompasses an area shown in Figure 2b. A dotted contour outlines the Y-feature as shown in Figure 1a. In each panel, star symbols indicate the positions of different star-forming regions, and the scale bar referring to 35 pc (at a distance of 2.0 kpc) is shown.

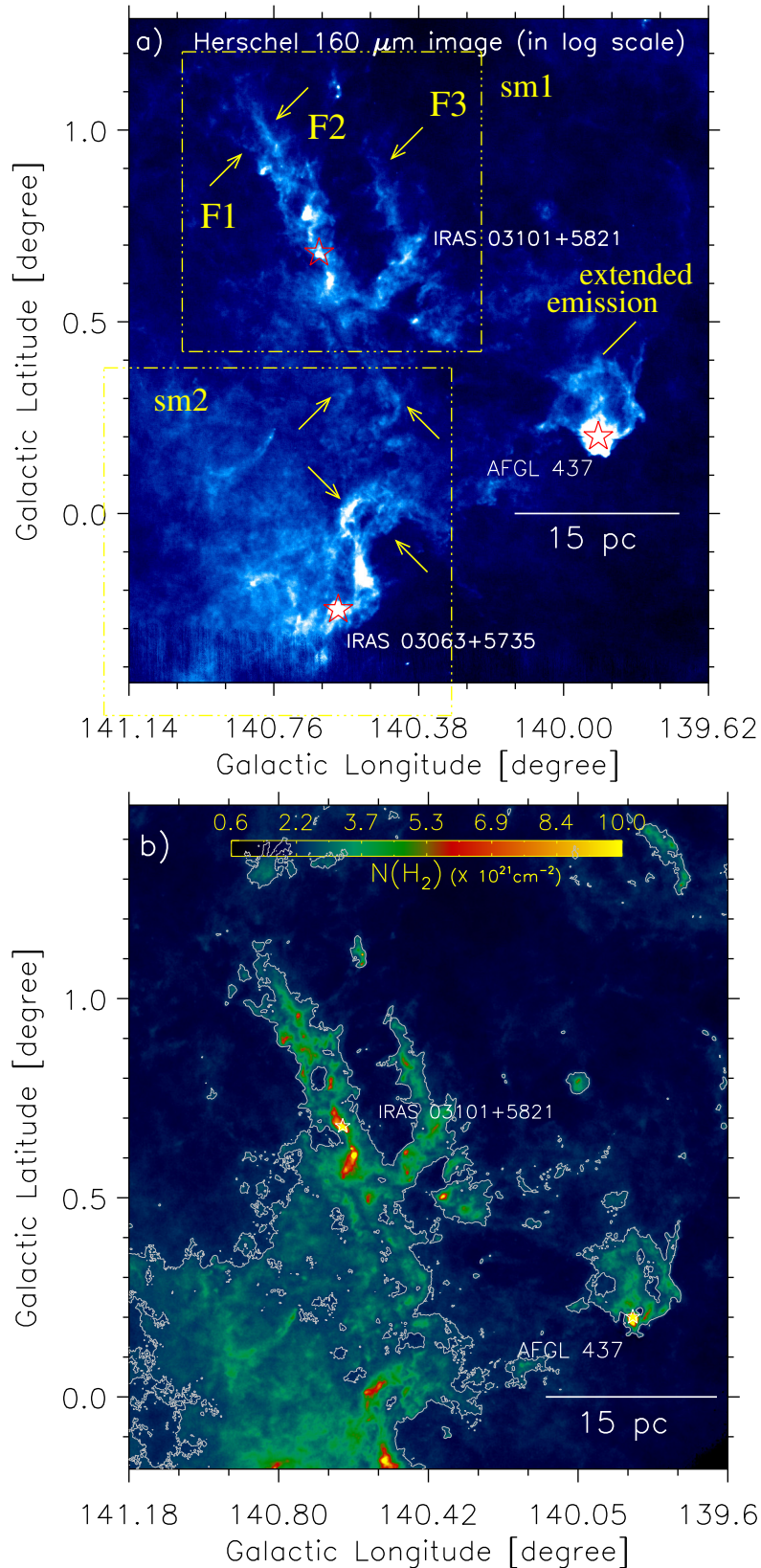


Figure 2. a) *Herschel* continuum image at 160 μm of an area highlighted by a dotted-dashed box in Figure 1b. Arrows highlight embedded filaments. Two subregions (i.e., sm1 and sm2) are highlighted by dotted-dashed boxes. b) *Herschel* column density ($N(\text{H}_2)$) map of an area highlighted by a solid box in Figure 1b. The column density contour (in gray) is also shown with a level of $2.4 \times 10^{21} \text{cm}^{-2}$. In each panel, star symbols are the same as in Figure 1a.

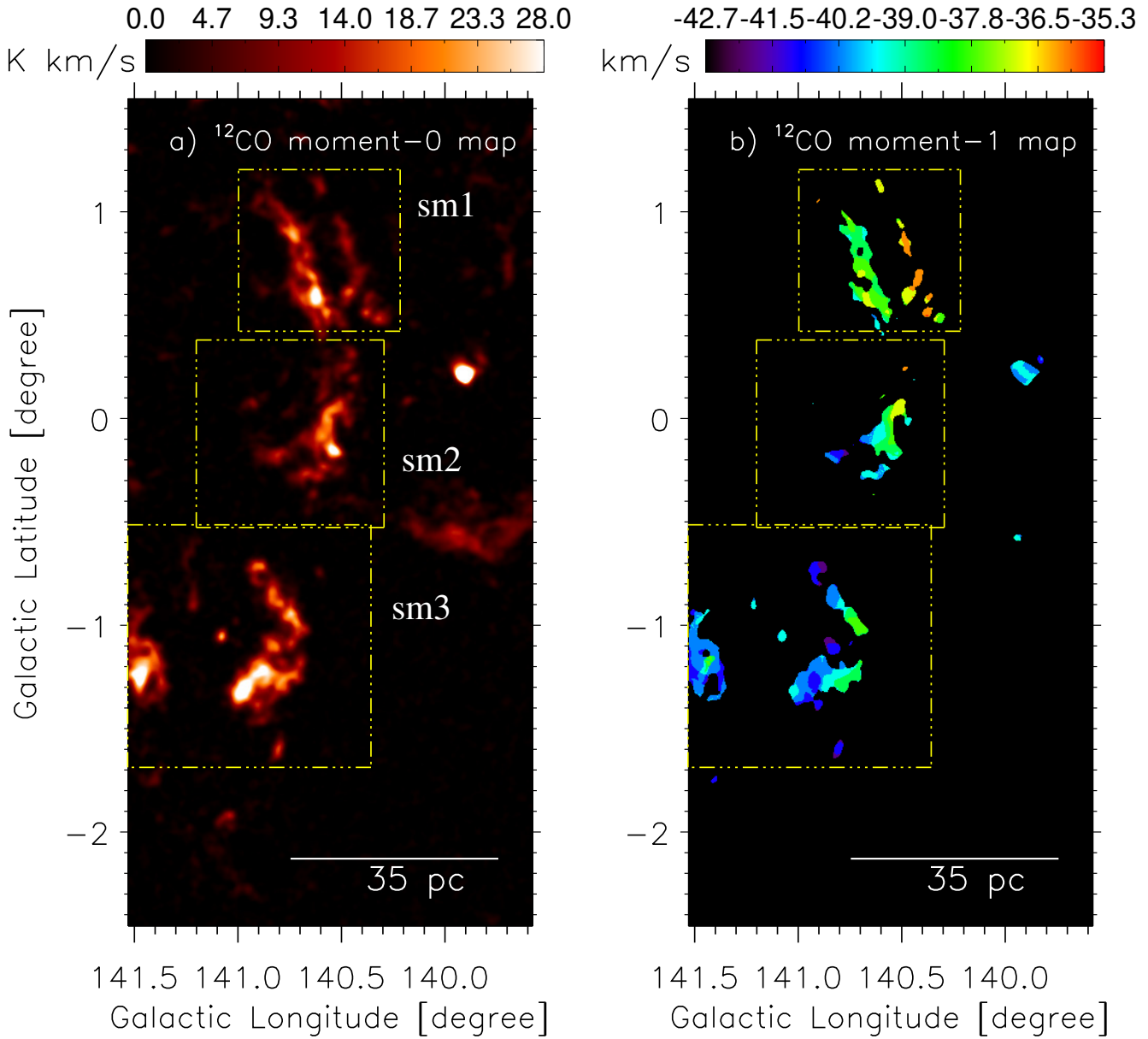


Figure 3. a) The CGPS $^{12}\text{CO}(1-0)$ molecular emission map (moment-0 map) toward the Y-feature. The molecular emission is integrated over a velocity range of $[-42.7, -34.4]$ km s^{-1} . b) The $^{12}\text{CO}(1-0)$ moment-1 map. In each map, three subregions sm1, sm2, and sm3 are indicated by dotted-dashed boxes.

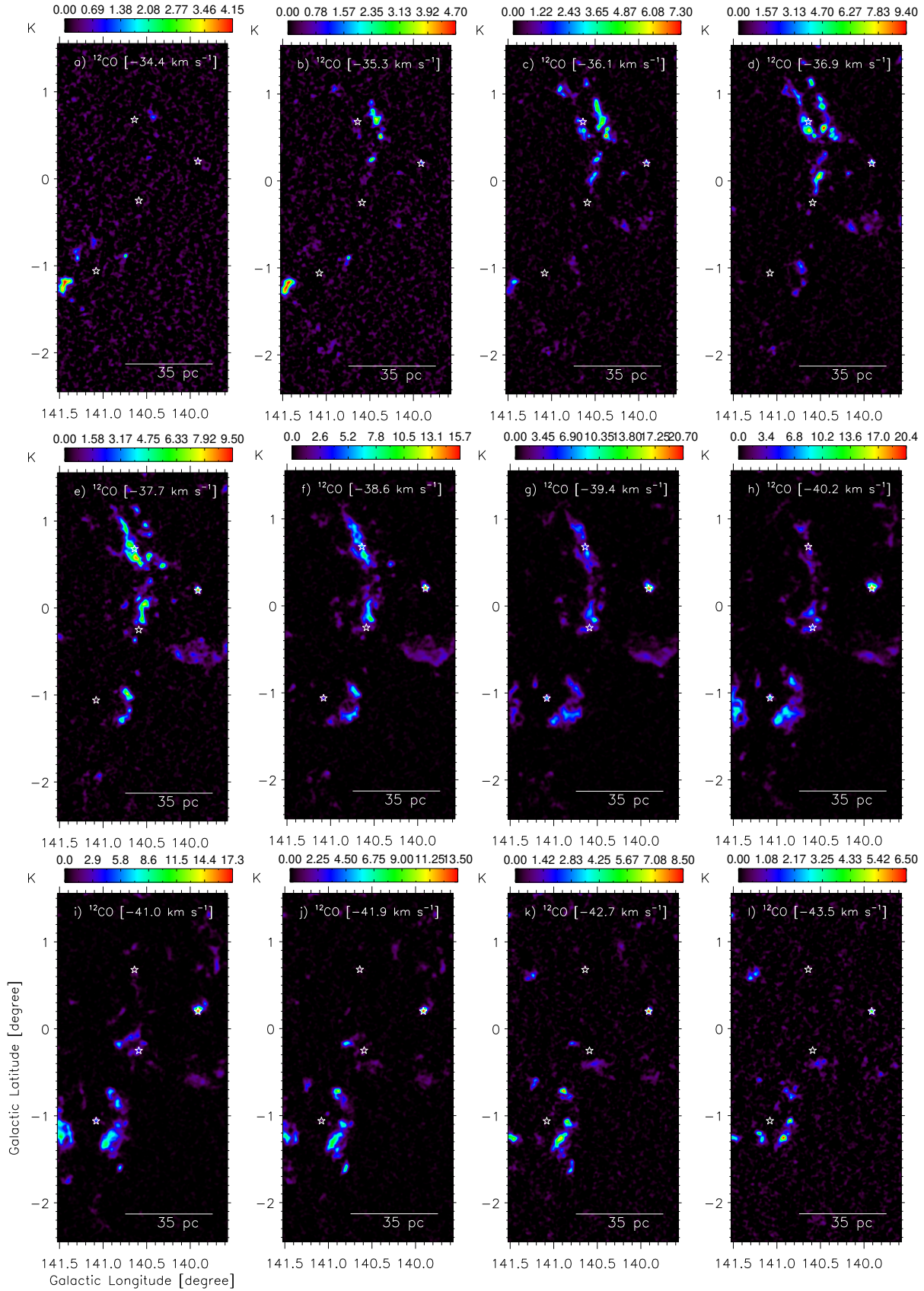


Figure 4. Velocity channel maps of the $^{12}\text{CO}(1-0)$ emission toward the Y-feature. The velocity of molecular emission is indicated in each panel (in km s^{-1}). In each panel, the scale bar and star symbols are the same as in Figure 1b.

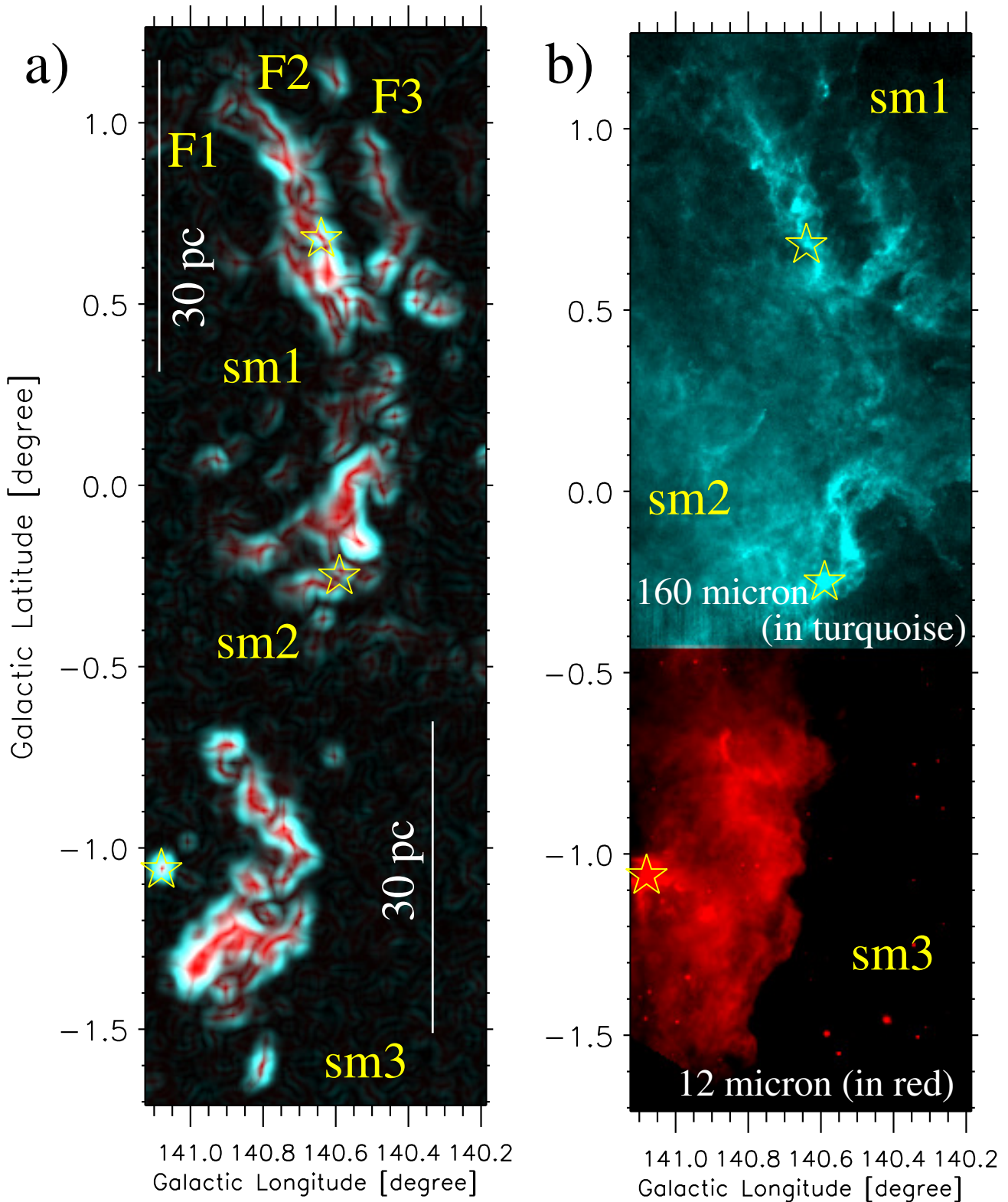


Figure 5. a) The panel shows a two-color composite image made using the $^{12}\text{CO}(1-0)$ moment-0 map. In the color composite image, the “sobel” processed $^{12}\text{CO}(1-0)$ moment-0 map is shown in red color, while the $^{12}\text{CO}(1-0)$ moment-0 map is displayed in turquoise color. The sobel filter is employed for edge detection (see text for more details and also Sobel 2014). b) The panel presents the infrared image toward Y-feature. The *Herschel* 160 μm image (in turquoise color) is shown toward subregions sm1 and sm2, while the WISE 12 μm image (in red) is displayed toward the subregion sm3. In each panel, star symbols are the same as in Figure 1a.

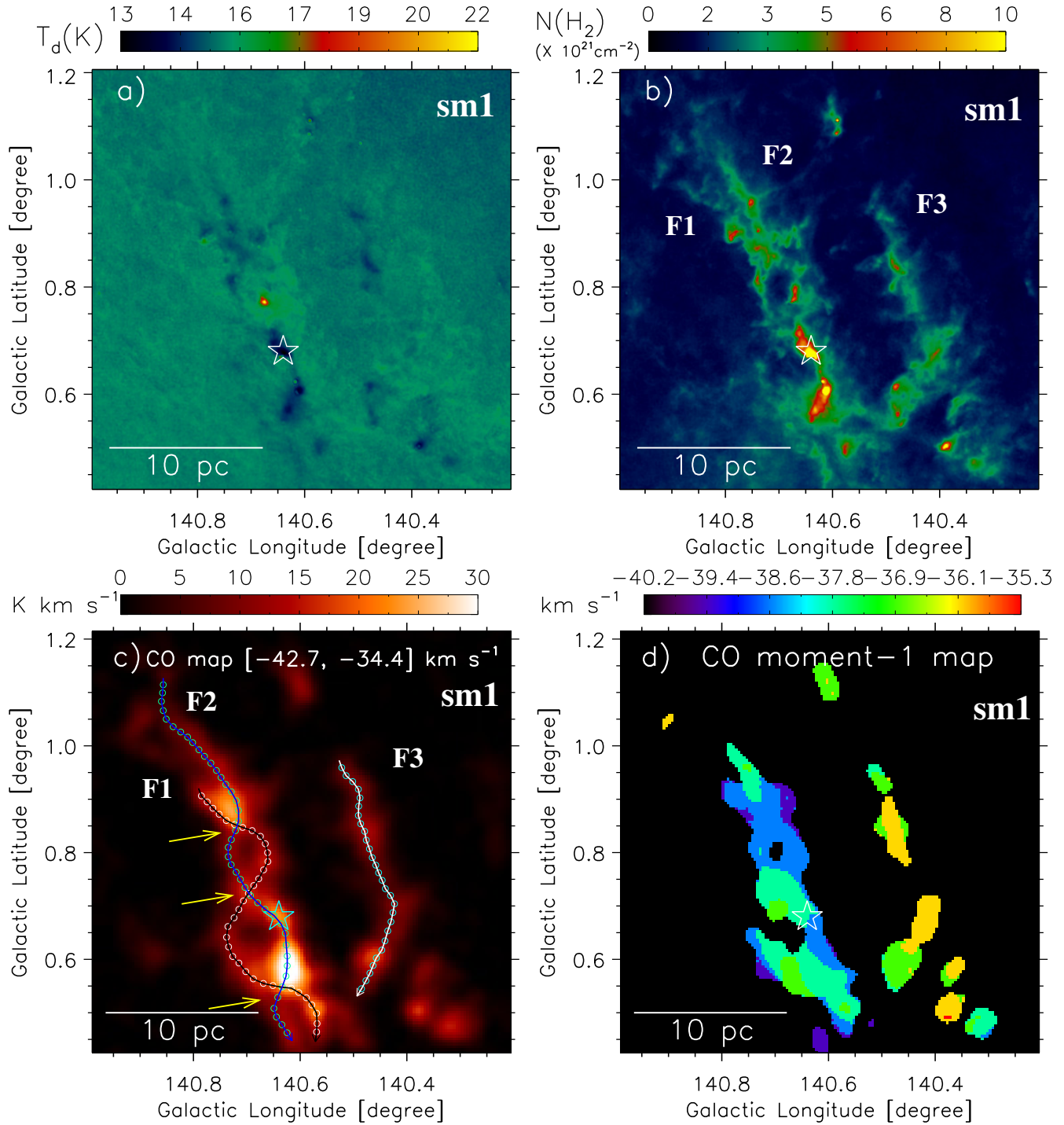


Figure 6. a) *Herschel* temperature map of the subregion “sm1” (see a dotted-dashed box in Figure 3a). b) *Herschel* column density map of “sm1”. c) The $^{12}\text{CO}(1-0)$ emission (moment-0) map of “sm1” (see Figure 3a). Three Filaments (i.e., F1, F2, and F3) are highlighted by curves. Several small open circles (radii = $20''$) are also marked along each filament, and an average spectrum over each circle is examined. Arrows highlight the common zones of the filaments F1 and F2. d) The $^{12}\text{CO}(1-0)$ moment-1 map of “sm1” (see Figure 3b). In each panel, the star symbol is the same as in Figure 1a.

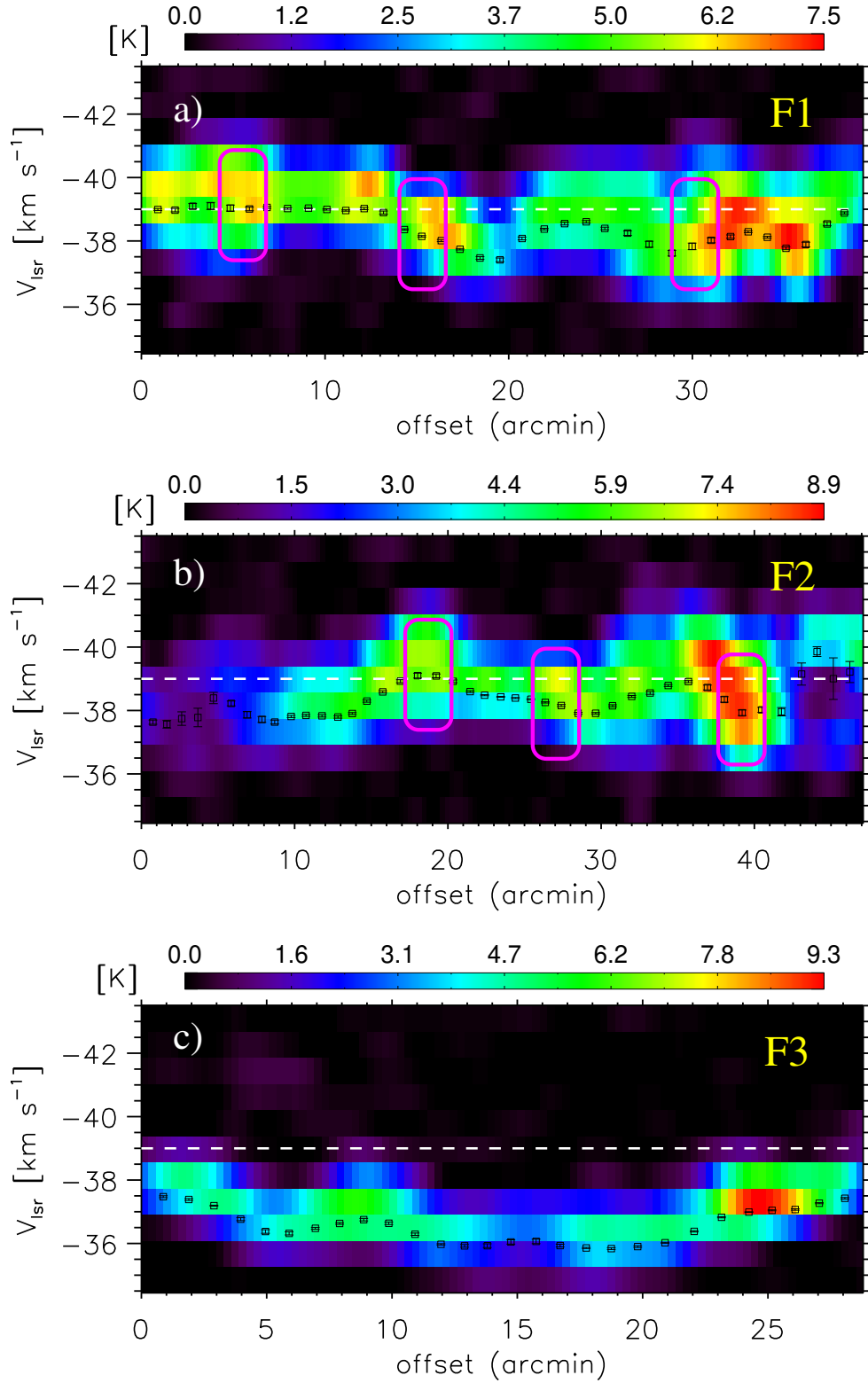


Figure 7. Position-velocity diagrams along the filaments a) “F1”, b) “F2”, and c) “F3” as indicated in Figure 6c. In panels “a” and “b”, pink boxes represent the common zones of the filaments F1 and F2 (see also arrows in Figure 6c). In all panels, black squares show mean velocities (along with error bars) derived through the Gaussian fitting of averaged spectra over circular regions (see small open circles in Figure 6c). In each panel, one arcmin ($1'$) corresponds to 0.58 pc (at a distance of 2 kpc), and a horizontal dashed line (in white) is marked at $V_{\text{lsr}} = -39 \text{ km s}^{-1}$.

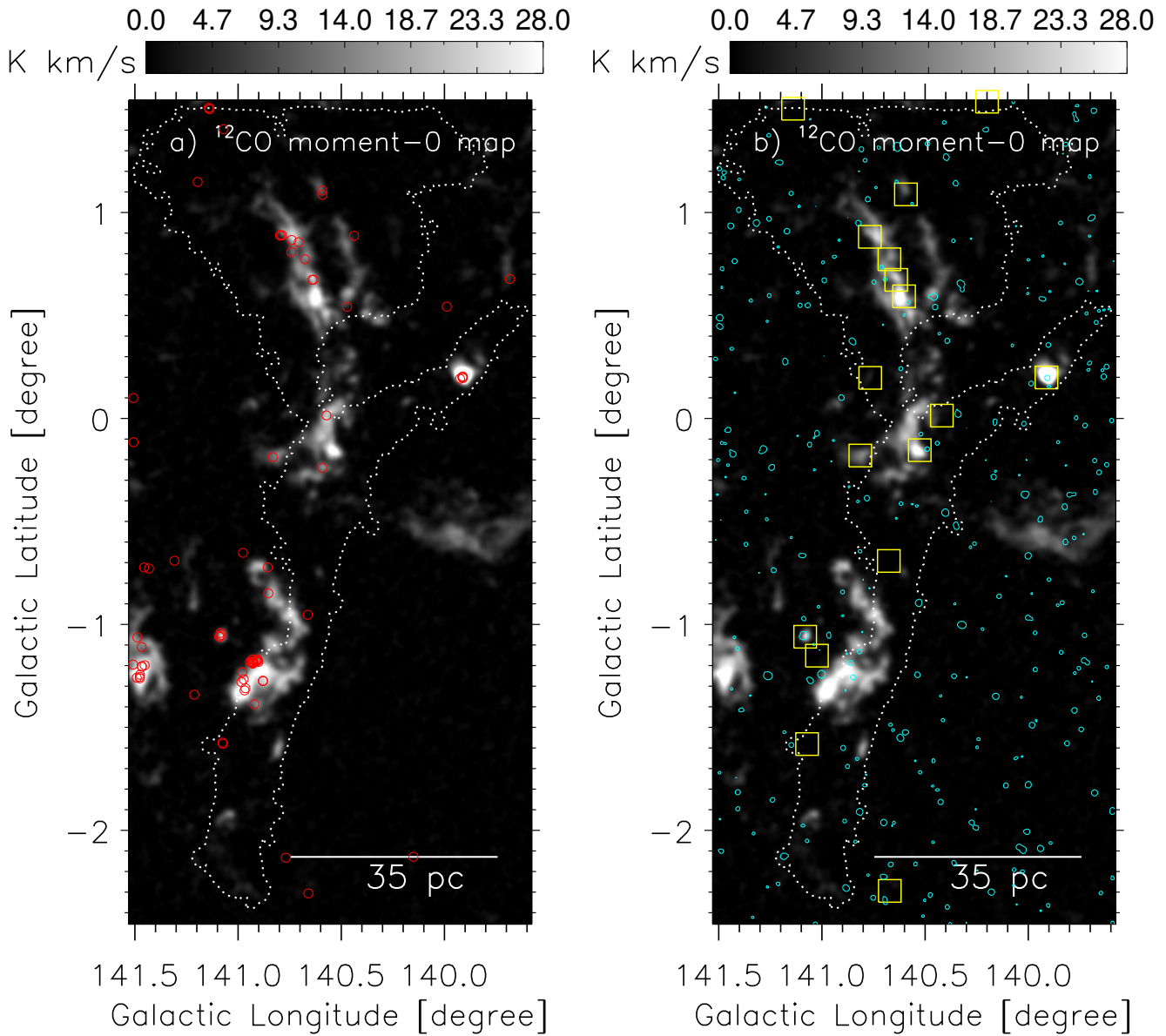


Figure 8. a) Overlay of the positions of infrared-excess sources (with $H-K > 1.3$ mag; see open circles) on the $^{12}\text{CO}(1-0)$ emission map. b) Overlay of the locations of YSOs presented in Karr & Martin (2003a) (see open squares) and the NVSS 1.4 GHz continuum emission contour on the $^{12}\text{CO}(1-0)$ emission map. The NVSS contour (in cyan) is also shown with a level of 5σ , where $1\sigma = 0.45$ mJy beam $^{-1}$. In both panels, the molecular map is the same as shown in Figure 3a. In each panel, the dotted contour showing the Y-feature and the scale bar are the same as in Figure 1b.